Facile synthesis, structure, and battery-type behavior of graphene oxides

J. M. D. Silva[1], F. P. M. Fenandes[2], M. de O. Silva[2], T. G. Maraschin[3],
L. S. Ferreira[1], D. A. Macedo[1], L. B. da Silva[1], F. de C. Fim[1]*
[1]Materials Science and Engineering Postgraduate Program,
Federal University of Paraíba, 58051-900, João Pessoa, PB, Brazil
[2]Department of Materials Engineering, Federal University of Paraíba, João Pessoa, PB, Brazil
[3]Technology and Materials Engineering Postgraduate Program,
Pontifical Catholic University of Rio Grande do Sul, Porto Alegre, RS, Brazil

Abstract

Graphene oxide (GO) is one of the main precursors for the production of graphene and other graphene-based materials. We report a simple, safe, and fast synthesis method to obtain graphene oxide as a functional material for battery-type electrodes. Washing and lyophilization processes were performed to evaluate their effects on exfoliation and removal of functional groups from graphene sheets. Sample GO1 consisted of a 10-layer stack of oxidized graphene, while sample GO2 had 8 stacked layers. The difference between them was an extra washing and lyophilization process in the GO2 sample. The electrochemical performance of graphene oxide-based electrodes, classified as battery-type, indicated an improved specific capacity of 10.15 $C.g^{-1}$ for GO1 against 4.55 $C.g^{-1}$ for GO2 at a specific current of 0.5 $A.g^{-1}$. This superior battery-type behavior of the GO1 electrode, also confirmed by electrochemical impedance spectroscopy, was most likely due to a higher degree of oxygenated groups on its surface, as shown by energy dispersive spectroscopy (EDS) and Fourier transform infrared spectroscopy (FTIR) studies.
Keywords: graphene oxide, chemical synthesis, microstructure, electrochemical performance, battery-type electrodes.

INTRODUCTION

Since Novoselov and Geim managed to isolate a single layer of graphene, showing the excellent properties of this material [1], graphene research has not stopped further. This has undoubtedly become the most studied area of interest in the last two decades, not only for the properties of graphene but also for the versatility of this material in combining with other elements to form graphene-based compounds [2]. One of the main synthesis routes of graphene-related materials involves graphene oxide (GO). The graphite oxidation process, which results in graphite oxide, with the help of strong oxidants, introduces functional groups such as carbonyls, epoxides, hydroxyl, and carboxyl groups that may be present on the edges and/or in the basal planes of the graphene layers [3]. These groups decrease the interactions between the layers, increasing the distance between them. The greater space between the graphene sheets helps in exfoliation, leading to the formation of a monolayer or a few layers of graphene oxide [4]. Therefore, GO is a graphene layer decorated with functional groups. These functional groups are responsible for the ease of functionalization of graphene sheets and their interaction with other materials [5]. This versatility of GO through chemical/thermal modifications alters its properties and makes it applicable in the most diverse areas, such as polymeric composites

[6], photocatalysis [7], membranes for water purification [8], sensors [9], supercapacitors [10] among others. Among those early mentioned applications, graphene oxide has attracted extensive interest in the field of devices for energy storage, particularly as a supercapacitor [11, 12], and is due to the effect of attached oxygen-containing functional groups present on the edges and/or in the basal planes of the graphene layers [3, 5, 11]. Supercapacitors, in turn, are energy-storage devices with long cyclic lives, quick charge-discharge rates, and high power densities when compared to batteries [11-13]. Based on their charge storage mechanism, supercapacitors can be classified into three main categories such as electrical double-layer capacitors (EDLC), pseudocapacitors, and battery-type behavior [13, 14]. Battery-type behavior energy-storage devices are those materials that store charge based on redox reactions and show intense and clearly separated oxidative and reductive peaks in their cyclic voltammetry and constant-current charge/discharge curves with plateaus in their galvanostatic charge-discharge cycles [14-17].

The first publication regarding the synthesis of graphite oxide was made by Brodie [18] in 1859 when he was studying the reactivity of the graphite flake. Brodie added potassium chlorate ($KClO_3$) to a slurry of graphite and fuming nitric acid (HNO_3) and determined that the material resulting from this reaction was made up of carbon, hydrogen, and oxygen, which provided an increase in the overall mass of graphite. Furthermore, he found that successive oxidation processes increased the oxygen content until reaching a limit after four consecutive reactions. In 1898, Staudenmaier [19] improved

---
*fabianafim@ct.ufpb.br
https://orcid.org/0000-0002-6339-1710

Brodie's protocol by using concentrated sulfuric acid (H_2SO_4) to increase the acidity of the mixture, in addition to fuming nitric acid and potassium chlorate. The change was due, in addition to the addition of another acid, to the addition of chlorate in multiple aliquots during the reaction. This modification of the procedure made it possible to obtain highly oxidized graphite oxide in a single step, making it no longer necessary to carry out consecutive oxidation reactions to reach a high oxygen content. This made the procedure more practical [19, 20]. In 1958, Hummers and Offeman [21] published the synthesis of graphite oxide with a strong oxidant that is potassium permanganate ($KMnO_4$), $NaNO_3$, and concentrated H_2SO_4; this made the oxidation process a little safer by not releasing ClO_2 [20, 21]. After a big gap in the graphite oxidation procedures to reach graphene oxide, Marcano et al. [20] published in 2010 a method called the improved Hummers method. In this method, the researchers excluded $NaNO_3$ and worked with a mixture of sulfuric and nitric acids, in addition to increasing the amount of $KMnO_4$, so there is no longer the generation of toxic gases, and the synthesis temperature is easily controlled [20]. The vast majority of procedures used today for the production of graphene oxide are based on the Hummers method without sodium nitrate, to make the process safer [3, 20]. It is important to note that until the publication of Hummers, it was considered graphite oxide because there was no appreciable exfoliation of the oxidized graphene sheets, maintaining a relevant number of stacked layers. Nowadays, some auxiliary operations for exfoliation are used, such as ultrasonication of graphite oxide in solution for the complete separation of graphene, resulting in a monolayer or few layers of graphene oxide [3].

We report a facile, safe, and fast approach for synthesizing graphene oxide. The herein proposed synthesis method provides to obtain an aqueous solution of graphene oxide suitable for drying by freeze-drying (GO1). Washing and freeze-drying processes are performed to provide a graphene oxide sample (GO2) with better exfoliation. To the best of our knowledge, no reports currently exist on the use of this synthesis route for the preparation of graphene-related compounds. The samples were characterized by Fourier transform infrared spectroscopy (FTIR), Fourier transform infrared spectroscopy by attenuated total reflectance (FTIR/ATR), X-ray diffraction (XRD), and Raman spectroscopy. The morphology was inspected by field emission scanning electron microscopy (FESEM) and transmission electron microscopy (TEM). In addition, we also report here the electrochemical assessment of graphene oxide-based electrodes toward energy storage as battery-like electrodes, which was performed at room temperature in a three-electrode cell configuration in an alkaline (3 M KOH) solution.

EXPERIMENTAL

Materials: flake graphite (9950, Nacional de Grafite, Minas Gerais, Brazil, purity 99.4%), sulfuric acid (H_2SO_4, 98%), potassium permanganate ($KMnO_4$), hydrogen peroxide (H_2O_2, 30%), polytetrafluoroethylene (PTFE, Merck, Brazil, 60 wt% dispersion in H_2O), and commercial Ni foam (QiJing, China, Ni 99.8%, porosity ~95%,) were used. All chemicals were of analytical reagent grades (Synth, Brazil) and used as received, without further purifications. The aqueous solutions were prepared with deionized water.

Graphene oxide synthesis: natural graphite flakes (NGF) were oxidized based on the modified Hummers method with some modifications [22]. Initially, a mixture containing 100 mL of H_2SO_4 and 8 g of $KMnO_4$ was prepared and mechanically stirred at around 400 rpm for 10 min. The mixture was placed in a water bath at 50 °C and 1 g of NGF was slowly added, keeping stirring for a further 2 h. At the end of this process, the solution was diluted in 500 mL of deionized water and taken to centrifugation at a rotation of 2000 rpm for 15 min. The solid removed was then washed again (twice) using the same conditions until reaching the pH of deionized water. After washing the material, the solid was placed in a beaker containing 1 L of deionized water and taken to magnetic stirring. A solution containing 25 mL of H_2SO_4 and 25 mL of H_2O_2 was prepared, added to the beaker, and stirred for 45 min at room temperature. Finally, the material was taken to the centrifuge (2000 rpm/15 min) and, after removing the existing solid, the same washing process mentioned above was performed twice more. Drying of the resulting material was carried out by freeze-drying. This material was named GO1. The GO1 that did not dry, that is, after the freeze-drying process, remaining as a gel, was again washed in the centrifuge and taken to freeze-drying. This second material was called GO2. Therefore, the GO2 sample went through the same initial processes to obtain the GO1 sample, however, it had an extra wash and underwent another drying by freeze-drying.

Characterizations: X-ray diffractograms were generated in a diffractometer (D8 Advance Davinci, Bruker) under CuKα radiation (0.154 nm), 40 kV, and 40 mA, with a Ni filter, analyzing at a velocity of 0.6 °/min, a step of 0.02°, in an angular range 6-60°. The interlamellar distance (d_{002}) was calculated by Bragg's law. The crystal size (C) which corresponded to the stacking of graphene layers was calculated using the Scherrer equation:

$$C = \frac{0.9\,\lambda}{\beta.\cos\theta} \qquad\qquad (A)$$

where λ is the wavelength used, β is the line width at half height in radians, and θ is the diffraction angle. The number of graphene layers was calculated by dividing the crystal size (C) by the interlayer distance (d), added to the thickness of one graphene sheet (0.1 nm) [4]. For Raman spectroscopy, the powder was tested in a spectrophotometer (inVia Micro-Raman, Renishaw) using an Ar laser with 20 mW of power and a wavelength (λ_L) of 532 nm (E_L=2.33 eV). A 50x objective lens was used, and the spectra were obtained in the region of 100 to 3000 cm^{-1}. The distance between the defects (L_D, nm) and the density of defects (n_D, cm^{-2}) by Raman spectroscopy was calculated by [23]:

$$L_D^2 = (1.8 \pm 0.5) \cdot 10^{-9} \, \lambda_L^4 \left(\frac{I_D}{I_G} \right)^{-1} \qquad \text{(B)}$$

$$n_D = \frac{(1.8 \pm 0.5) \cdot 10^{22}}{\lambda_L^4} \left(\frac{I_D}{I_G} \right) \qquad \text{(C)}$$

where λ_L is the laser wavelength (nm), and I_D/I_G is the D to G band intensity ratio. The FTIR/ATR assays were performed with a spectrophotometer (IR Prestige-21, Shimadzu) with the following conditions of analysis: region 4000-600 cm^{-1}; resolution: 4 cm^{-1}; number of accumulation: 20; mode: transmittance. GO samples were also analyzed at 25 °C as pellets diluted in KBr by transmission FTIR spectroscopy, using the FTIR spectrophotometer, with an accumulation of 20, in the 4000-400 cm^{-1} range. Scanning electron microscopy (SEM) analyses were performed with a microscope (Leo 1430, Zeiss) operating at 15 kV. The samples were prepared by deposition of the powdered material on carbon tape and metalized with gold. Energy dispersive X-ray spectroscopy (EDS) was performed using a field emission scanning electron microscope (FESEM, Inspect F50, FEI) operating at 20 kV and equipped with a spectrometer. For transmission electron microscopy (TEM) analysis, the samples remained 1 h in an ultrasonic bath (45 kHz) in acetone and were further deposited on copper grids. TEM images were obtained using a microscope (JEM-2010, Jeol) operating at 200 kV.

Electrochemical characterization: electrochemical measurements were conducted using a potentiostat/galvanostat (Autolab PGSTAT204, Metrohm) with FRA32 M module in a three-electrode cell containing the working electrode, a counter electrode (blank and pressed Ni foam 2x2 cm) and a reference electrode (Ag/AgCl) in a 3 M KOH electrolyte at room temperature. A homogeneous slurry, consisting of 80 wt% of active material (powder of GO1 or GO2), 10 wt% of polytetrafluoroethylene (PTFE), and 10 wt% of carbon black, in 500 mL isopropyl alcohol was used to prepare the working electrodes. Then, the inks containing each powder were drop-casted on Ni foams (1x1 cm) and further heated at 373 K for over 12 h in a vacuum to remove residual solvent. The mass loading of the active material on Ni foam was ~5 mg.cm^{-2}. Cyclic voltammetry (CV) was performed between 0 and 0.5 V vs. Ag/AgCl at scan rates ranging from 5 to 100 mV.s^{-1}. A blank Ni foam was also studied under the same conditions for comparison. The galvanostatic charge-discharge (GCD) test was conducted in a potential window of 0-0.45 V at a current ranging from 0.5 to 10 A.g^{-1}. Electrochemical impedance spectroscopy (EIS) was carried out in the frequency range of 0.1 to 10 kHz at a constant potential of 0.35 V vs. Ag/AgCl with a voltage amplitude of 5 mV.

RESULTS AND DISCUSSION

Structural properties of graphene oxide: the crystal structures of the natural graphite flake (NGF) and graphene oxide (GO) samples obtained by the synthesis methods were investigated by X-ray diffractometry. Fig. 1 shows the XRD patterns of NGF, GO1, and GO2. The NGF sample showed two characteristic graphite peaks, referring to the (002) and (004) planes in 2θ at approximately 26° and 54°, respectively. The highest intensity peak, corresponding to the (002) plane, represents the axial plane c, perpendicular to the hexagonal graphite planes. Through the diffractograms of the GO samples, it was possible to observe that the peak around 26° disappeared and a new peak formed at approximately 10°, as a result of the oxidation process. This newly formed XRD peak was referred to as the (001) plane of the hexagonal crystal structure of graphene oxide [24]. Therefore, GO1 and GO2 samples had peaks and basal distances characteristic of graphene oxide [25]. It is worth noting a small peak found in the GO1 sample at 2θ=25.30°. This peak, not found in the GO2 sample, is characteristic of graphite, which can be justified by the existence of the remaining starting material [26]. This indicated that the additional washing process can remove all material that was not oxidized. The data taken from the diffractograms, such as interlamellar distance (d), full width at half maximum (FWHM), crystal size (C), and the number of stacked graphene sheets (#graphene) are listed in Table I. All these parameters refer to the (002) axial plane of the crystal structure of the NGF sample, and to the (001) plane for the GO1 and GO2 samples.
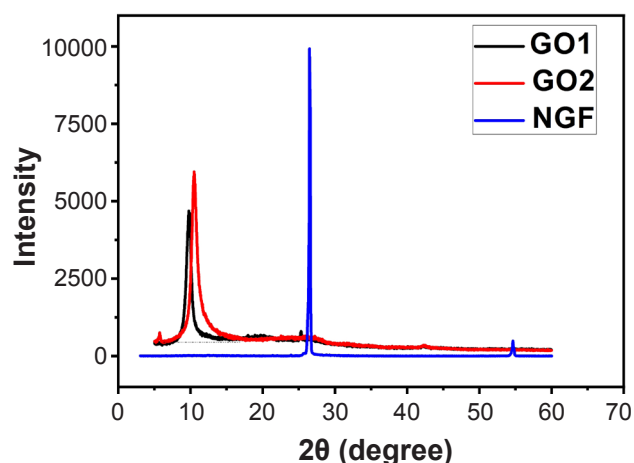

Figure 1: X-ray diffractograms of natural graphite flake (NGF) and graphene oxide (GO1 and GO2) samples.

From Table I, it can be seen that the process of obtaining GO1, which consisted of oxidation, washing, and centrifugation with subsequent freeze-drying, was sufficient to achieve a stack of up to 10 graphene sheets. However, the oxidation time was not enough to break all π-π bonds in the bulk of the material, indicating the difficulty of diffusing the oxygen groups into the graphene sheets. According to Chung [27], the graphene layers are bound in the axial direction by weak van der Waals forces produced by a delocalized π orbital. This delocalization stabilizes the carbon bond in the plane (the carbons that form the graphene layer), so the bond strength is greater than that of a single covalent C-C bond. So if all these weak van der Waals bonds were broken, the material would have a monolayer. However,

Table I - XRD parameters for natural graphite flake (NGF) and graphene oxide (GO1 and GO2) samples.

Sample	2θ (degree)	d (nm)	FWHM (rad)	C (nm)	#graphene
NGF	26.51	0.3362	0.0034	44.09	131
GO1	9.75	0.9072	0.0161	9.03	10
GO2	10.55	0.8386	0.0214	6.82	8

this did not occur in our work, and it is possible to suggest that oxygen groups were present, preferentially at the edges of the slides. It should be noted that the crystal sizes were relatively large, equal to 9.03 and 6.82 nm for the GO1 and GO2 samples, respectively. But this was due to the presence of the oxygenated groups that contributed to this size, as well as being responsible for the increase in the interlamellar distance in agreement with Chung [27]. Furthermore, it was possible to verify that the additional washing step performed on the GO2 sample did not show a significant difference in the material structure. However, with an additional washing process, the GO2 particles could be reassembled, but after freeze-drying these particles were dispersed again [28]. As the #graphene in the GO2 sample was slightly smaller than in GO1, it can be stated that the freeze-drying process is quite efficient in separating the graphene layers because the low-pressure freezing and the solvent sublimation produce a very stable and dispersed solid structure [29]. Trikkaliotis et al. [30] also synthesized GO by a very similar route, but with a quantity of starting graphite ten times greater (10 g) than that used in the present study, which resulted in a GO with a crystal size greater than 12.11 nm and a number of graphene layers from 13 to 14. This showed that the amount of graphite used in the synthesis also influences the crystallite size and the number of stacked graphene.

Fourier transform infrared spectroscopy: FTIR is a technique widely used to differentiate the functional groups present in the structure of materials. The most common ways of analyzing samples of carbon-based materials are by transmission, where the infrared beam is transmitted through the sample, therefore the sample must be dispersed in potassium bromide (KBr) and by reflection as the attenuated total reflectance (ATR), where no sample preparation is required and the measurement is taken directly. As the infrared beam is reflected by the crystal, its penetration into the sample is superficial [31]. Therefore, the main difference between these two analysis modes is due to the interaction of the infrared beam with the sample. In transmission FTIR the beam interacts with the entire sample, from the surface to the bulk, while in FTIR/ATR the beam interacts much more with the surface of the sample. Fig. 2 shows the FTIR spectra through the transmitted beam and the attenuated total reflectance infrared (FTIR/ATR) spectra of NGF, GO1, and GO2 samples. The peak around 3400 cm^{-1} represents O-H stretching and the peak at 2918 cm^{-1} represents C-H asymmetric axial strain. The bands related to the carbonyls (C=O) and aromatic rings (C=C) are shown at 1730 and 1628 cm^{-1}, respectively. Besides, the band at 1411 cm^{-1} was assigned with the deformations of OH from the COOH groups [32]. And finally, C-O bonds in the band at 1037 cm^{-1}
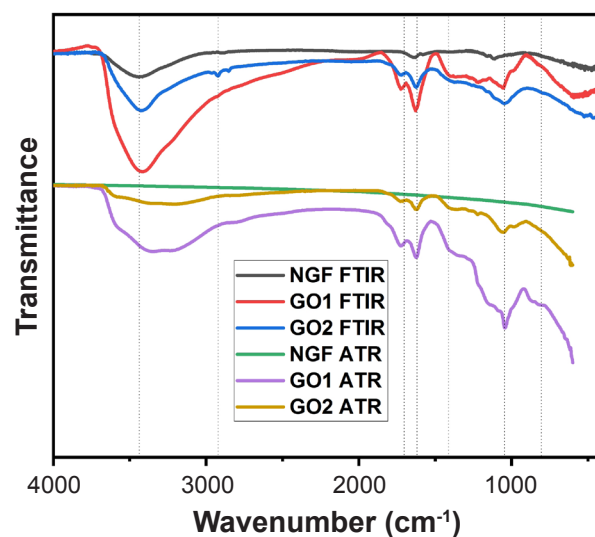

Figure 2: FTIR/ATR and transmitted-beam FTIR spectra of NGF, GO1, and GO2 samples.

and =C-H bonds at 812 cm^{-1} were observed. All these bands are characteristic of a graphene oxide sample [24].

The additional washing did not influence the types of oxygen groups found in the samples either by FTIR/ATR or by transmitted beam FTIR, indicating the strong bond with the graphene structure. It was seen that the intensities of the bands of these groups were quite variable and did not follow a trend. The shape of the OH band at 3400 cm^{-1} was shown to be very wide when FTIR/ATR was performed, characteristic of OH carboxylic acid, and when the transmitted beam analysis was performed, there was a decrease in peak broadening, more characteristic of the OH of the residual water. Therefore, it can be assumed that the carboxylic acid was more present on the surface of the GO, mainly on the edges of the graphene sheets, than in the bulk, and this is understandable since this group is quite voluminous. In addition, there was another difference in the spectra obtained by FTIR/ATR and transmitted beam that concerned the characteristic groups of the graphitic structure, C=C of aromatic, C-H, and =C-H. Of these, only C=C was visualized in both analysis modes, but it appeared more intensely on the GO surface. The C-H group was present only in transmitted beam analyses, therefore it was present only in the GO bulk. This can be explained by the fact that on the surface there was more presence of oxygenated groups and also more edge defects, which could reduce the presence of these C-H groups. It is still possible to indicate that on the surface of the GO, there was a greater presence of epoxy groups, OH, and carbonyl groups.

Raman spectroscopy: is considered a very efficient tool

to characterize the structure of graphitic materials. The main characteristic peaks of these materials are the G, D, and 2D bands. The peak referring to the G band comes from the elongation of the C-C band and is common to all materials that contain sp^2 carbon atoms in their structure [33]. The D band is related to the lattice symmetry breaking due to the presence of defects, and the 2D band (second order of the D band) is a double resonance process, that is two consecutive propagation events that happen as induced by the disorder. The 2D band is responsible for providing information about the number of graphene layers [34, 35]. Fig. 3 presents the Raman spectra of the natural graphite flake (NGF) and synthesized graphene oxide samples (GO1 and GO2). Table II presents the data referring to the Raman results after the deconvolution of the D and G peaks for the GO samples (inserts in Fig. 3). These bands were fitted by two symmetrical lines (D and G bands) by Gaussian function after applying the baseline to the curves.
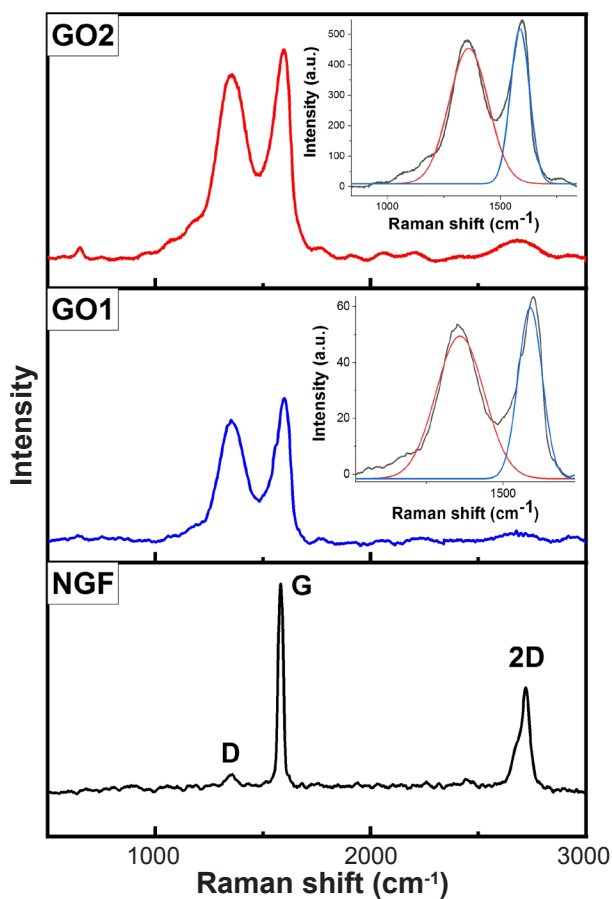

Figure 3: Raman spectra of the natural graphite flake (NGF) and synthesized graphene oxide samples (GO1 and GO2).

The adjusted parameters were the position and intensity of the bands. The natural graphite flake (NGF) sample showed a peak at around 1349 cm^{-1}, referring to the D band, and a much more intense peak at around 1574 cm^{-1} referring to the G band. Fig. 3 shows that NGF had few defects in relation to the graphitic structure, that is, there was a predominance of sp^2 carbon. If the NGF sample was crystalline and free of defects, there would be no D band in the spectrum [36]. Concerning the GO samples, it was possible to verify that after the NGF oxidation, there was a displacement of the D and G bands to 1359 and around 1588 cm^{-1}, respectively. There was also a very significant increase in the intensity of the D band (Fig. 3), as a result of the increase in sp^3 carbon. All these Raman shifts are characteristic of graphitic samples and showed that the oxidation process introduced many structural defects, which occurred due to the presence of functional groups [37].

According to Wei et al. [37], graphene oxide presents high intensities for both the D and G bands, and the ratio between these intensities I_D/I_G (also known as disorder parameter [38]) was used to evaluate the amount of defects in GO samples. As shown in Table II, the I_D/I_G ratios of the GO samples were much higher than that of the NGF, which confirmed its low number of defects. The GO2 sample had more defects than GO1, showing that the additional washing and drying process can lead to an increase in the number of defects, not being enough to lead to a greater separation between the graphene layers. This result was in agreement with that observed in the XRD analysis, which showed a small amount of difference with respect to the #graphene sample. In addition to the increase in the intensity ratio I_D/I_G, the defect density (n_D) is another parameter that also confirmed the increase in defects in the GO2 sample (Table II). Cançado et al. [23] showed how to calculate the distance between defects (L_D) and the density of defects (n_D) for all laser lines in the visible range for graphene samples. It is worth mentioning that Eqs. B and C are used for point-type defects, such as vacancies, substitutional atoms, etc., as these defects can activate the D-band in the Raman process. Defects such as intercalating agents and deformations in the lattice, for example, have a strong influence on the G and 2D bands, but not on the D band [23]. In the present work, the L_D and n_D results were presented for the graphite and GO samples (Table II). It was observed that there was no significant difference between the samples of GO1 and GO2, the latter having presented a slight decrease in the distance between the defects, as well as an increase in the density of defects. This greater number of defects verified in the GO2 sample is explained by the surface defects, which appeared as holes in the graphene

Table II - Raman parameters for natural flake (NGF) and graphene oxides (GO1 and GO2).

Sample	D-band (cm^{-1})	G-band (cm^{-1})	2D-band (cm^{-1})	I_D/I_G	L_D (nm)	n_Dx10^{11} (cm^{-2})
NGF	1349	1574	2705	0.19	27	0.44
GO1	1359	1588	2700	0.83	13	1.87
GO2	1359	1586	2698	0.87	12	1.96

layers, being possible to verify these holes in the SEM and TEM images that are shown later. Therefore, we can consider that both GO1 and GO2 samples had active point defects for the D band besides defects from the functional groups. Another important consideration from Cançado et al. [23] is that Eq. B can only be used for L_D values ≥10 nm and Eq. C for L_D>10 nm, which is in agreement with the values found for GO1 and GO2. Concerning the 2D band of the samples, it was possible to verify that there was a very accentuated difference in the band shape (Fig. 3) and position (Table II). The NGF presented a band with two distinct components, while in the samples GO1 and GO2, the band was quite wide. This clearly showed that the oxidation process significantly altered the shape of this band, as already described by Ferrari [39], as a result of interactions proved by the functional groups that caused a lot of disorder in the graphene layers. The position of this 2D band was also closely linked to the number of graphene layers that the sample had, as this number decreased, the band shifted to higher frequencies [39].

Scanning electron microscopy: Fig. 4 shows SEM images of NGF with a structure of bright scales, which was also observed by Ni et al. [35]. It was possible to identify that the NGF was formed by parallel layers. In addition, the distance between the layers was imperceptible, looking like a single layer. It was only after the oxidation process that this material experienced an increase in the spacing between these layers, as shown in the XRD analysis. Fig. 5 shows SEM images of the GO1 sample. It was seen the corrugation defects that are characteristic of this type of material due to the presence of functional groups. Another factor was the overlapping of its layers (Fig. 5a), in which the material presented the layers separated as also observed by Park and Ruoff [40] without the sample having gone through any additional process for their separation. Fig. 5b shows smooth

surfaces with wrinkles and folded regions, characteristic of GO. According to Al-Gaashani et al. [24], this aspect is the result of sp^3 carbons and structural defects. The image of Fig. 5c shows the presence of holes, indicated by red arrows, in the oxidized graphene layers, as the presence of these point defects has already been discussed by Raman spectroscopy. The EDS analysis (Fig. 5d) performed from the image of Fig. 5c showed the presence of sulfur (S) and manganese (Mn) indicating that the washing process was not efficient in removing all the reagents used during the oxidation. The C/O ratio can be understood as a measure that serves as a reference for the degree of oxidation of GO. In the present work, it was possible to calculate this ratio as 1.22. According to Compton et al. [41], GO normally has a C/O ratio below 2, suggesting that the lower this ratio, the greater the degree of oxidation.

Fig. 6 presents the SEM images and EDS spectrum of the GO2 sample. This material showed the same characteristics of GO1, however, with a very accentuated distribution of defects. These defects can be visualized in Fig. 6a signaled by the red arrows as holes found along the graphene sheets. This may have occurred due to the second freeze drying to which the material was subjected since GO2 had a smaller thickness than GO1 (confirmed by XRD), proving to be more fragile and the removal of water under vacuum twice may have inserted these defects. In the image of Fig. 6b, it is possible to verify that the material was very thin, with a transparent appearance. In the image of Fig. 6c, one can see that the layers of oxidized graphene were quite separate from each other. This Fig. 6c served as the basis for the EDS spectrum shown in Fig. 6d. From the table inserted in Fig. 6d, it is possible to verify that there was a significant decrease in sulfur (S) and manganese (Mn) residues from the oxidizing agents and the aluminum that come from the stub where the sample was deposited. The C/O ratio found for
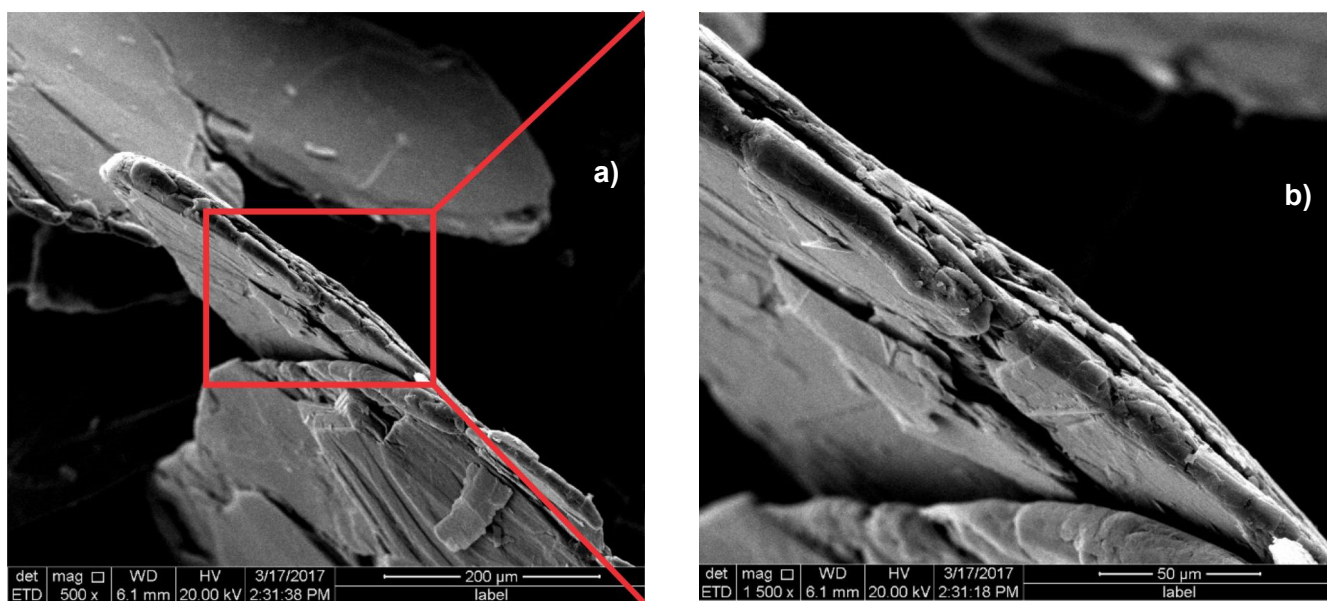

Figure 4: SEM images of the natural graphite flake (NGF) at different magnifications.
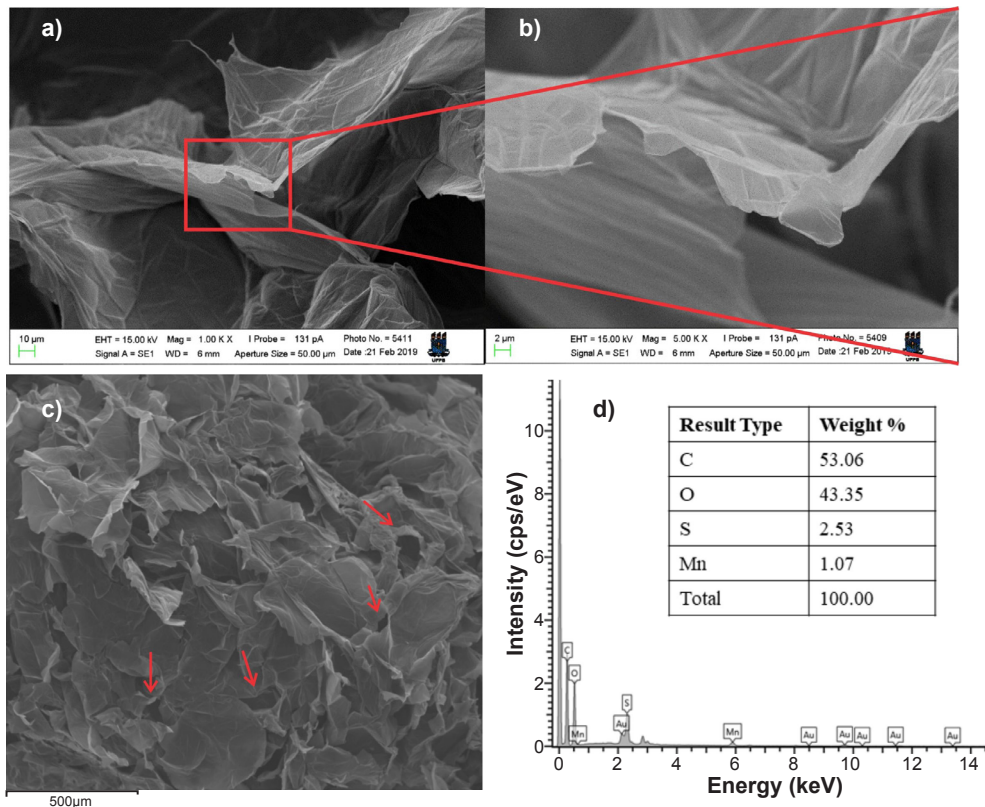
Figure 5: SEM images of the GO1 sample at different magnifications (a-c) and EDS spectrum with a table showing the elements' contents found in the sample.
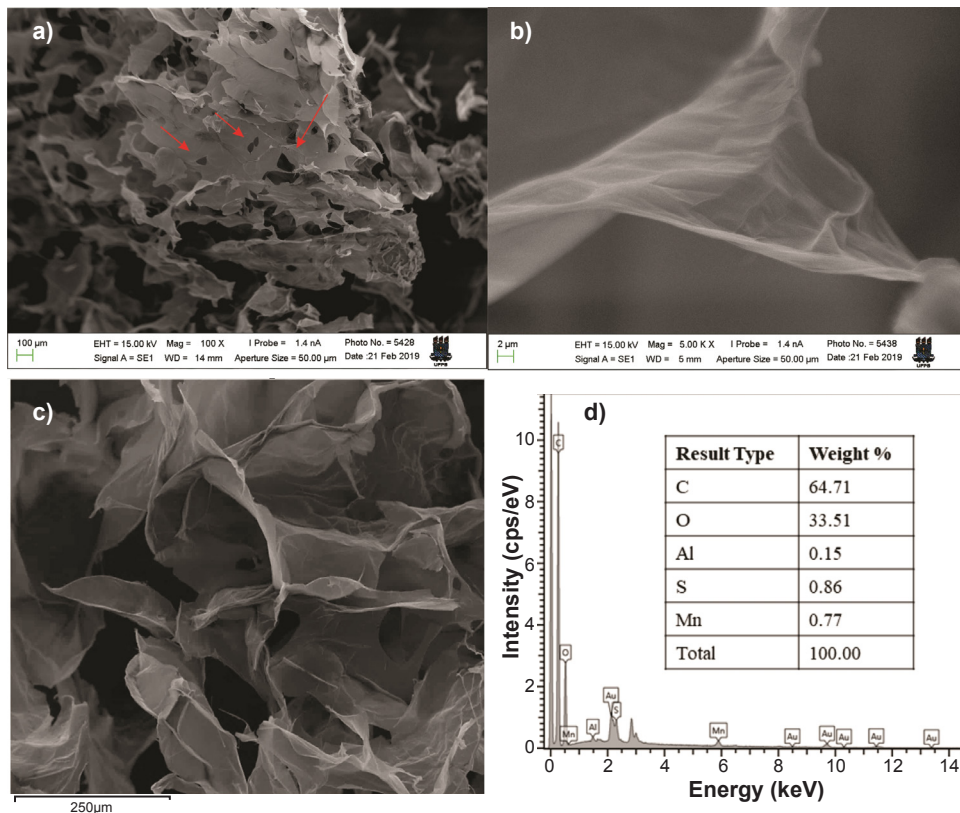
Result Type	Weight %
C	53.06
O	43.35
S	2.53
Mn	1.07
Total	100.00

Figure 6: SEM images of the GO2 sample at different magnifications (a-c) and EDS spectrum with a table showing the elements' contents found in the sample.

Result Type	Weight %
C	64.71
O	33.51
Al	0.15
S	0.86
Mn	0.77
Total	100.00

the GO2 sample was 1.93, which indicated a lower degree of oxidation compared to the GO1 sample (C/O=1.22). This result was in agreement with the FTIR data that showed a lower intensity of oxygenated groups in the GO2 structure.

Transmission electron microscopy: it is possible to verify the TEM images of the GO1 and GO2 samples in Fig. 7. The images show a lot of folds, both in GO1 and GO2, but in both samples there was certain transparency, indicating the small stacking of graphene sheets in agreement with Stobinski et al. [42]. In GO2, it can be seen a difference in contrast (inside the red circle) most likely due to the hole defect in the blades because it is possible to see small folds where it is lighter, that is, it shows that there were folded edges.

Electrochemical study: electrochemical performance of as-resulted materials toward supercapacitive behavior was measured by using a three-electrode system in a 3 M KOH electrolyte at room temperature. Fig. 8 displays the results of cyclic voltammetry (CV) of graphene oxides (GO1 and GO2) at different scan rates (5-100 mV.s^{-1}). The anodic/cathodic profile peaks of both samples showed that their intensities increased as the scan rate also increased, which remained the CV curves unaltered over the entire scan rate range. This event revealed good kinetics reversibility of the OH$^-$ ions, improved mass transport, and fast electronic/ionic transport rates that demonstrated good stability of the alkaline electrolyte with the graphene oxide-based electrodes [43]. Also, according to the CV profiles, these samples could be classified as battery-type behavior materials [15, 16, 44], since the electrode polarization effect, shown by the presence of two redox peaks (for both samples) indicated that the charge storage process was mainly governed by a surface faradaic redox mechanism [15, 16, 44].

Taking into account the presence of Mn in both GO1 and GO2 samples, according to previously evidenced by EDS studies, the mechanism of the redox reaction for these GO electrodes may be related to the presence of reversible valence Mn^{3+}/Mn^{4+} state [45]. Besides, the residual S in graphene samples, also evidenced by EDS, could improve its capacitive behavior to increase the charge density of the state and the electrode wettability [46]. Anyway, the basic and acidic graphene character can be modified by the presence of metal transition and/or heteroatoms which can enhance its redox activity [13]. In addition, the Ni foam contribution for the GO (GO1 and GO2) supercapacitive performance was not significant as the CV area of Ni foam was very small when compared to CV profiles of the GO electrodes (Fig. 8c). The larger area of the CV curve showed by the GO1 electrode suggested a higher charge storage capability. From CV curves, it can also be obtained the relationship between the current peak (i_p) and the square root of scan rate ($v^{1/2}$). Fig. 8d shows a linear ($R^2{\geq}0.99$) relation for both GO1 and GO2 samples, being the slopes ($b=i_p/v^{1/2}$) equal to 103 and 40 for anodic and -73 and -29 for cathodic currents, respectively. This linear relation also confirmed the battery-type behavior of the samples and indicated that the energy storage process was controlled by diffusion-limited reactions [43, 47]. These results indicated that the GO1 sample had faster rates of reversible surface redox reactions when compared to the GO2 electrode. This was most likely due to a higher degree of oxygenated groups on the surface of the GO1 sample, as showed by EDS and FTIR analyses, although GO1 was thicker than G2, which was in accordance with previous works [48-50]. It is well known that the presence of oxygenated groups enhances the adsorption ability of OH$^-$ ions, accelerating the redox reaction rate [14].

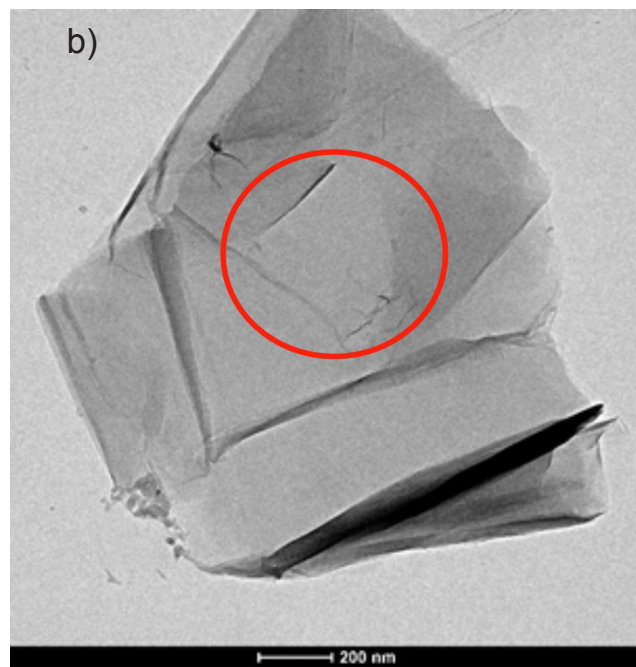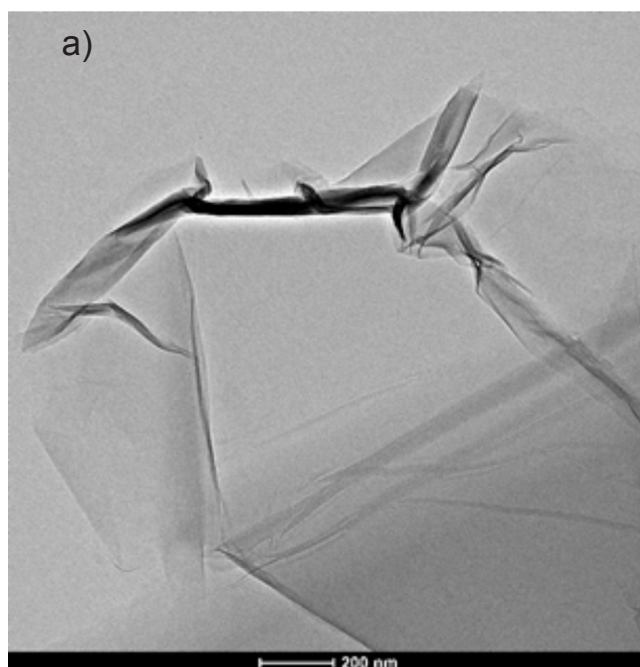Fig. 9 shows the galvanostatic charge-discharge (GCD)

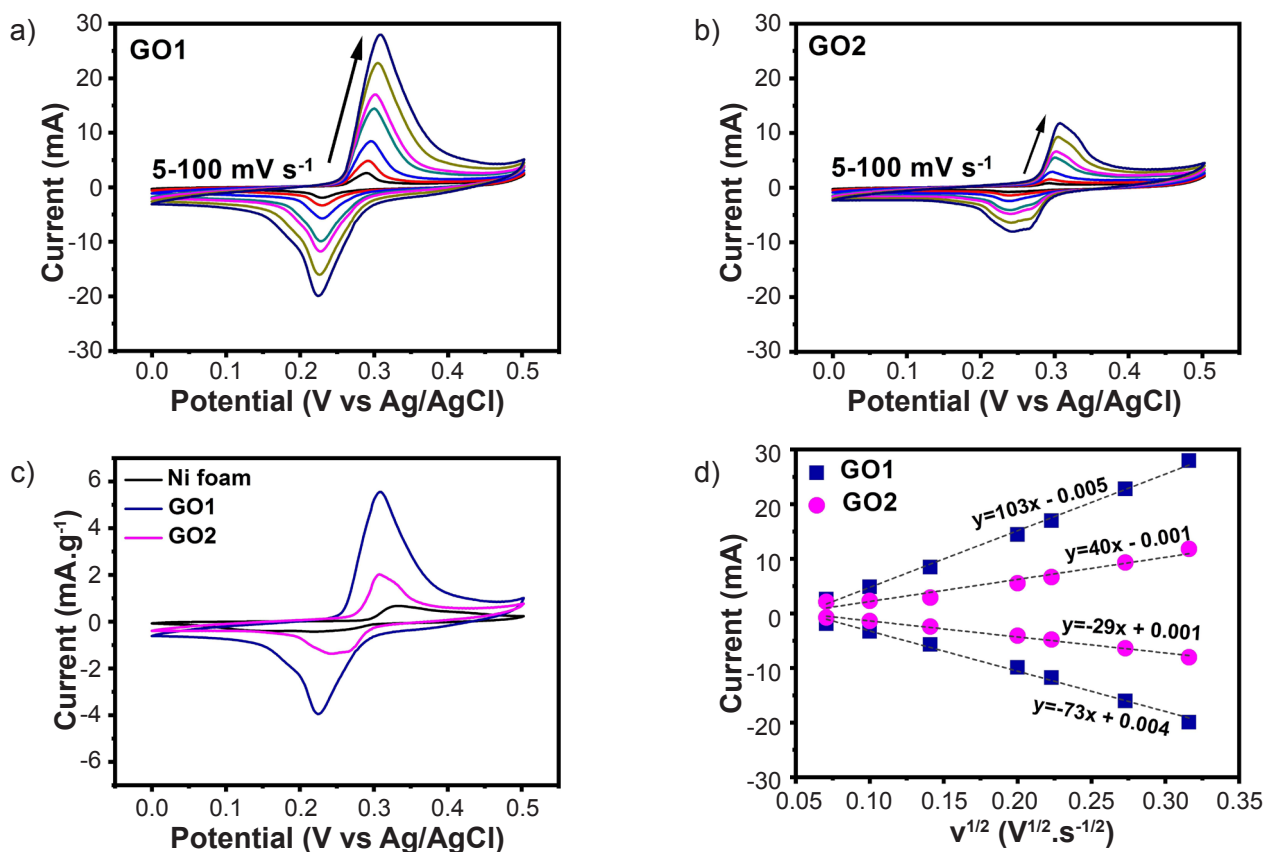Figure 7: TEM images of GO1 (a) and GO2 (b) samples.

Figure 8: CV profiles of GO electrodes acquired between 0-0.5 V at scan rates ranging from 5 to 100 mV.s^{-1} of GO1 (a) and GO2 (b), comparison of CV curves recorded at 100 mV.s^{-1} (c), and plots of peak current vs. square root of scan rate, with scan rates ranging from 5 to 100 mV.s^{-1} (d).
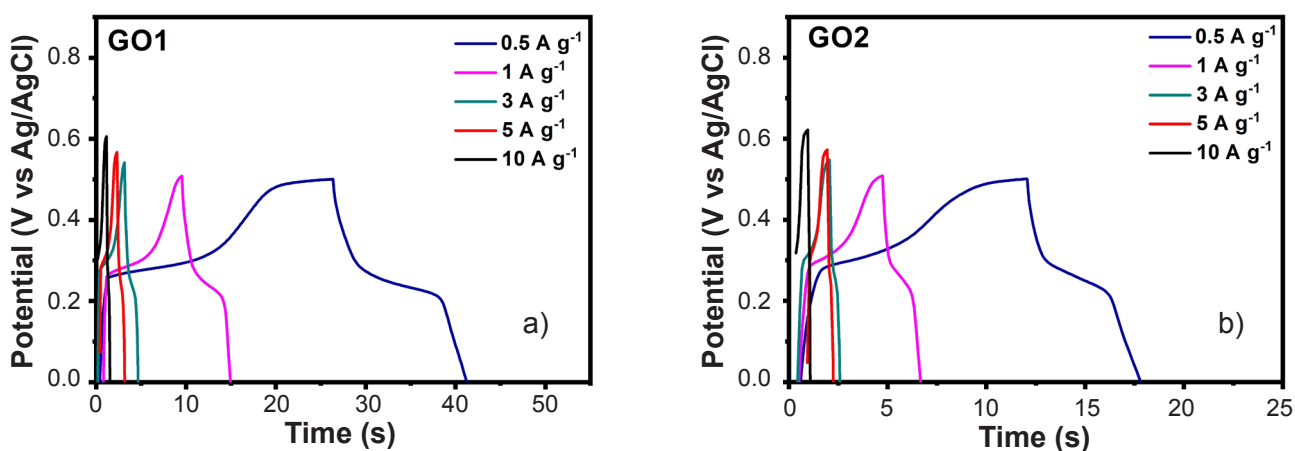

Figure 9: Galvanostatic charge-discharge (GCD) curves of GO1 (a) and GO2 (b) samples.

results of the GO-based electrodes. According to the GCD curves, a characteristic non-linear (potential plateaus), typical of Faradaic reactions, confirmed again the battery-type behavior of the GO-based electrodes [15, 16]. For battery-type behavior, the specific capacity (Qs) of the electrodes should be calculated using the following equation:

$$Qs = I.\frac{\Delta t}{m} \qquad\qquad (D)$$

where I is the discharge current (A), Δt is the discharge time (s), and m is the mass of the active material (g) [47, 51]. In this way, the C.g^{-1} was adopted as the metric for the specific capacity of the GO-based electrodes. As shown in Fig. 10, the GO1 electrode had the highest specific capacity (10.15 C.g^{-1}) at 0.5 A.g^{-1} against 4.55 C.g^{-1} for GO2 at the same specific current.

Electrochemical impedance spectroscopy (EIS) analyses were also conducted to investigate the performance of GO-
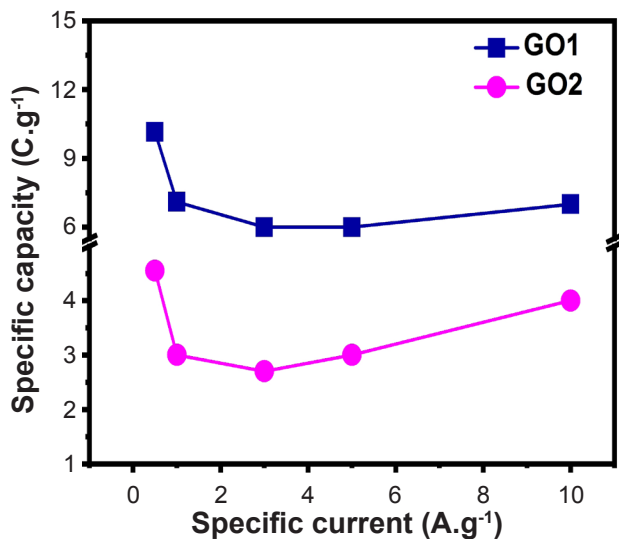
Figure 10: Specific capacity at specific currents ranging from 0.5 to 10 A.g^{-1}.
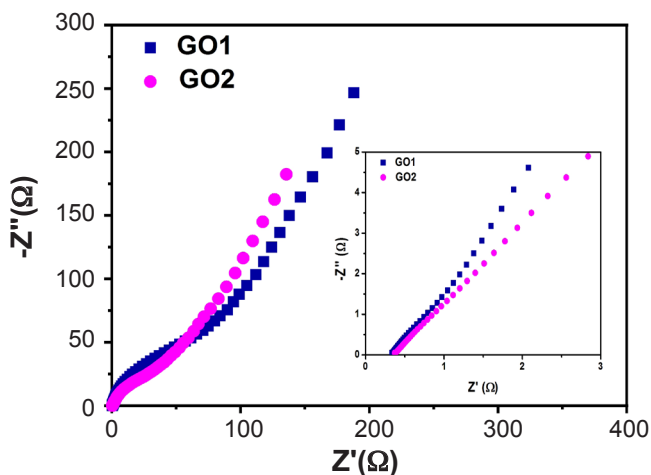

Figure 11: Nyquist plots of GO1 and GO2 samples recorded in 3 M KOH with insert showing the high-frequency region.

based electrodes. Nyquist plots of GO1 and GO2 samples are shown in Fig. 11. The high-frequency intercept on the real Z' axis (insert in Fig. 11) is related to the equivalent series resistance (ESR) which represents the total resistance of the active materials (intrinsic resistance of the electrode, the bulk electrolyte resistance, and the resistance at electrolyte/electrode interface) [13, 47]. The ESR values were determined to be 0.32 and 0.35 Ω for GO1 and GO2 electrodes, respectively. The reversibility of the adsorption-desorption of electrolyte ions is indicated by the semi-circles in the higher frequency region, and its diameter is related to the Faradaic charge transfer resistance (R_{ct}) of the materials [13, 47]. The R_{ct} values for GO1 and GO2 were, respectively, 6.35 and 7.13 Ω. The lower R_{ct} value found for the GO1 sample suggested faster kinetics on its surface, in good agreement with CV and GDC analyses.

CONCLUSIONS

This study showed that it is possible to safely and quickly obtain graphene oxide with up to 10 stacked layers without any exfoliation process (e.g., sonication) just using the freeze-drying method, leading to the denomination of graphene oxide with few layers. X-ray diffraction indicated that even with 10 layers of stacked graphene, the crystal size was large and this was due to the presence of functional groups bonded between the sheets. By FTIR-ATR and FTIR by transmission, it was possible to confirm the presence of carboxylic acid on the surface of the layers, while at the edges of the layers and in the bulk, the most significant presence was of OH coming from the residual water of the obtaining process. Also in both samples, the presence of carbonyls, OH, and epoxy both on the surface and in the bulk were found. Raman spectroscopy showed that the presence of surface defects from the functional groups affected the D, G, and 2D bands. These surface defects were most likely to be found in the GO2 sample, corroborating the SEM and TEM images. Therefore, both the additional washing and freeze-drying did not bring benefits that surpassed the results obtained in the GO1 sample, so it was not necessary to carry out another washing and freeze-drying. The electrochemical assessment allowed classifying GO1 and GO2 samples as functional materials for battery-type electrodes. The improved specific capacity of the GO1 sample was ascribed to a higher degree of oxygenated groups on its surface showing that oxygenic functional groups were found to be a significant factor of influence on the electrochemical supercapacitor performance of graphene oxide electrodes.

ACKNOWLEDGEMENTS

REFERENCES

[1] K.S. Novoselov, A.K. Geim, S.V. Morozov, D. Jiang, Y. Zhang, S.V. Dubonos, I.V. Grigorieva, A.A. Firsov, Science **306** (2004) 666.
[2] M.J. Allen, V.C. Tung, R.B. Kaner, Chem. Rev. **110** (2010) 132.
[3] M.F.R. Hanifah, J. Jaafar, M.H.D. Othman, A.F. Ismail, M.A. Rahman, N. Yusof, W.N.W. Salleh, F. Aziz, Materialia **6** (2019) 100344.
[4] G. Pavoski, T. Maraschin, F.C. Fim, N.M. Balzaretti, G.B. Galland, C.S. Moura, N.R.S. Basso, Mater. Res. **20**, 1 (2017) 53.
[5] S. Pei, Q. Wei, K. Huang, H.-M. Cheng, W. Ren, Nat. Commun. **9** (2018) 145.
[6] J.M.D. Silva, S.V.C.R. Coutinho, R.K.M. Diniz, A.N.F. Almeida, M.E.A. Lima, F.C. Fim, Macromol. Symp. **383**

(2019) 1800017.

[7] G.M. Neelgund, A. Oki, Appl. Surf. Sci. **566** (2021) 150648.

[8] T. Wu, F. Moghadam, K. Li, J. Membr. Sci. **645** (2022) 120216.

[9] X. Kang, R. Wang, M. Jiang, E. Li, Y. Li, X. Yan, T. Wang, Z. Ren, Opt. Fiber Technol. **68** (2022) 102807.

[10] R. Lakra, R. Kumar, P.K. Sahoo, D. Sharma, D. Thatoi, A. Soam, Carbon Trends **7** (2022) 100144.

[11] B. Xu, S. Yue, Z. Sui, X. Zhang, S. Hou, G. Cao, Y. Yang, Energy Environ. Sci. **4** (2011) 2826.

[12] Y.B. Tan, J.-M. Lee, J. Mater. Chem. A **1** (2013) 14814.

[13] D. Prakash, S. Manivannan, J. Alloys Compd. **854** (2021) 156853.

[14] T.R. Silva, V.D. Silva, L.S. Ferreira, A.J.M. Araújo, M.A. Morales, T.A. Simões, C.A. Paskocimas, D.A. Macedo, Ceram. Int. **46**, 7 (2020) 9233.

[15] Y. Gogotsi, R.M. Penner, ACS Nano **12** (2018) 2081.

[16] P. Simon, Y. Gogotsi, B. Dunn, Mater. Sci. **343** (2014) 1210.

[17] T.S. Mathis, N. Kurra, X. Wang, D. Pinto, P. Simon, Y. Gogotsi, Adv. Energy Mater. **9** (2019) 1902007.

[18] B.C. Brodie, Philos. Trans. R. Soc. Lond. **149** (1859) 249.

[19] L. Staudenmaier, Ber. Dtsch. Chem. Ges. **31**, 2 (1898) 1481.

[20] D.C. Marcano, D.V. Kosynkin, J.M. Berlin, A. Sinitskii, Z. Sun, A. Slesarev, L.B. Alemany, W. Lu, J.M. Tour, ACS Nano **4**, 8 (2010) 4806.

[21] W.S. Hummers Jr., R.E. Offeman, J. Am. Chem. Soc. **80** (1958) 1339.

[22] C. Li, Y. Shi, X. Chen, D. He, L. Shen, N. Bao, Chem. Eng. Sci. **176** (2018) 319.

[23] L.G. Cançado, A. Jorio, E.H.M. Ferreira, F. Stavale, C.A. Achete, R.B. Capaz, M.V.O. Moutinho, A. Lombardo, T.S. Kulmala, A.C. Ferrari, Nano Lett. **11** (2011) 3190.

[24] R. Al-Gaashani, A. Najjar, Y. Zakaria, S. Mansour, M.A. Atieh, Ceram. Int. **45** (2019) 14439.

[25] T.F. Emiru, D.W. Ayele, J. Basic Appl. Sci. **4**, 1 (2017) 74.

[26] C.J. Guerrero, B.F. Caballero, Mater. Chem. Phys. **153** (2015) 209.

[27] D.D.L. Chung, J. Mater. Sci. **37** (2002) 1475.

[28] Q. Li, J. Liu, A. Bai, P. Li, J. Li, X. Zhang, M. Yu, J. Wang, H. Sun, J. Chem. **2019** (2019) 1.

[29] C. Valencia, C.H. Valencia, F. Zuluaga, M.E. Valencia, J.H. Mina, C.D. Grande-Tovar, Molecules **23** (2018) 2651.

[30] D.G. Trikkaliotis, A.C. Mitropoulos, G.Z. Kyzas, Colloids Surf. A **600** (2020) 124928.

[31] D.G. Trikkaliotis, A.K. Christoforidis, A.C. Mitropoulos, G.Z. Kyzas, Chem. Eng. **5** (2021) 64.

[32] G. Shao, Y. Lu, F. Wu, C. Yang, F. Zeng, Q. Wu, J. Mater. Sci. **47** (2012) 4400.

[33] H.-H. Huang, K.K.H. Silva, G.R.A. Kumara, M. Yoshimura, Sci. Rep. **8** (2018) 6849.

[34] M.S. Dresselhaus, A. Jorio, M. Hoffman, G. Dresselhaus, R. Saito, Nano Lett. **10**, 3 (2010) 75.

[35] Z. Ni, Y. Wang, T. Yu, Z. Shen, Nano Res. **1**, 4 (2008) 273.

[36] L.G. Cançado, K. Takai, T. Enoki, Appl. Phys. Lett. **88** (2006) 163106.

[37] Y. Wei, Z. Pastuovic, T. Murphy, D.B. Gore, Appl. Surf. Sci. **505** (2020) 144651.

[38] C. Tyagi, S.A. Khan, S. Ojha, D.K. Avasthi, A. Tripathi, Vacuum **154** (2018) 259.

[39] A.C. Ferrari, Solid State Commun. **143** (2007) 47.

[40] S. Park, R.S. Ruoff, Nat. Nanotechnol. **4** (2009) 217.

[41] O.C. Compton, B. Jain, D.A. Dikin, A. Abouimrane, K. Amine, S.T. Nguyen, ACS Nano **5**, 6 (2011) 4380.

[42] L. Stobinski, B. Lesiak, A. Malolepszy, M. Mazurkiewicc, B. Mierzwa, J. Zemek, P. Jiricek, I. Bieloshapkada, J. Electron Spectrosc. Relat. Phenom. **195** (2014) 145.

[43] A.J.M. Araújo, V.D. Silva, A.R.O. Sousa, J.P.F. Grilo, T.A. Simões, D.A. Macedo, R.M. Nascimento, C.A. Paskocimas, Ceram. Int. **45** (2019) 7157.

[44] T. Brousse, D. Belanger, J.W. Long, J. Electrochem. Soc. **162** (2015) A5185.

[45] Y. Zhang, Y. Liu, Z. Sun, Y Bai, S. Cheng, P. Cui, J. Zhang, Q. Su, J. Fu, E. Xi, Electrochem. Acta **375** (2021) 137979.

[46] X. Yu, Y. Kang, H.S. Park, Carbon **101** (2016) 49.

[47] L.S. Ferreira, T.R. Silva, V.D. Silva, T.A. Simões, A.J.M. Araújo, M.A. Morales, D.A. Macedo, Adv. Powder Technol. **31** (2020) 604.

[48] M. Karbak, O. Boujibar, S. Lahmar, C. Autret-Lambert, T. Chafik, F. Ghamouss, C **8** (2022) 27.

[49] S. Lin, J. Tang, K. Zhang, Y. Chen, R. Gao, H. Yin, L.-C. Qin, Nanoscale Adv. **5** (2023) 1163.

[50] H. Cao, X. Peng, M. Zhao, P. Liu, B. Xu, J. Guo, RSC Adv. **8** (2018) 2858.

[51] J. Iqbal, A. Numan, S. Rafique, R. Jafer, S. Mohamad, K. Ramesh, S. Ramesh, Electrochim. Acta **278** (2018) 72.